IEEE Access
Multidisciplinary | Rapid Review | Open Access Journal

Received 22 July 2022, accepted 13 September 2022, date of publication 16 September 2022, date of current version 23 September 2022.

Digital Object Identifier 10.1109/ACCESS.2022.3207183

RESEARCH ARTICLE

A Methodology for High-Power Drives Emulation Using a Back-to-Back Configuration

FERNANDO BRIZ[1], (Senior Member, IEEE), MARIAM SAEED[1], (Member, IEEE), JUAN MANUEL GUERRERO[1], (Senior Member, IEEE), IGOR LARRAZABAL[2], DAVID ORTEGA[2], IBAN AYARZAGUENA[2], AND ANDONI PULIDO[2]

[1]Department of Electrical, Computer and System Engineering, University of Oviedo 33204 Gijón, Spain
[2]Ingeteam Power Technology S.A., Traction Research and Development, 48170 Zamudio, Spain

Corresponding author: Fernando Briz (fbriz@uniovi.es)

This work was supported in part by the European Commission H2020 under Grant UE-18-POWER2POWER-826417; in part by the Spanish Ministry of Science, Innovation and Universities under Grant MCIU-19-PCI2019-103490; and in part by the Government of the Principality of Asturias under Project AYUD/2021/50988.

ABSTRACT Validation of high-power converters at the development stage often cannot be performed using the real load. A testbench consisting of the Equipment Under Test (i.e., tested power converter) and an auxiliary power converter, preferably using power recirculation, can be used instead. A challenge for correct testing using this approach comes from the fact that the harmonic content of the currents can significantly differ between the testbench and the real system. This might strongly affect the loading of power switching devices compromising the reliability of the validation process. This paper proposes a methodology to select the operating conditions of both tested and auxiliary converters in the testbench to resemble a given operating condition of the actual system. Since identical behavior is not generally possible, a cost function will be used to trade-off among different factors (i.e., fundamental current magnitude and phase, harmonic content, etc.). The proposed approach evaluates a large number (hundreds of thousands) of testbench operating points in a few seconds and selects those which minimize the cost function. In a later stage, the selected points can be validated using detailed dynamic simulation. The selected conditions can then be used to test the converter in the testbench emulating the real system behavior in a given operating point condition. The proposed methodology was developed for railway electric drives but can be extended to other applications.

INDEX TERMS Railway traction drive, machine emulation, back-to-back inverters, current harmonics, power recirculation, high-power converter testbench.

NOMENCLATURE

v_a, v_b, v_c: phase voltages in the time domain.
$\vec{v}^{EUT}$: *EUT* complex vector voltage in the time domain.
$\vec{v}_f^{EUT}$: fundamental component of *EUT* complex vector voltage in the time domain.
$\vec{v}_h^{EUT}$: h^{th} harmonic component of *EUT* complex vector voltage in the time domain ($\omega_h = h\,\omega_f$).
$\vec{V}^{EUT}$: *EUT* voltage in the frequency domain.
$\vec{V}_f^{EUT}$: fundamental component of *EUT* voltage in the frequency domain.
$\vec{V}_h^{EUT}$: h^{th} harmonic component of *EUT* voltage in the frequency domain.
α^{EUT}: angle of fundamental component of *EUT* complex vector voltage.
φ: *EUT* power factor.

Same cases apply for currents by replacing v/V and i/I.

Same cases apply for *AUX* inverter by replacing *EUT* by *AUX*.

Variables denoted by prime refers to testbench parameters.

The associate editor coordinating the review of this manuscript and approving it for publication was Zhuang Xu.

I. INTRODUCTION

Validation of high-power converters at the development stage is a challenging task [1]. On one hand, often it cannot be performed using the real load. On the other, power

consumption and/or dissipation requirements might be unacceptable. These drawbacks can be overcome by using a testbench consisting of the Equipment Under Test, *EUT* (i.e., tested converter) and an auxiliary converter (i.e., *AUX*) in a back-to-back configuration as shown in Fig. 1. Real-time emulators such as Power Hardware-In-the-Loop and Power Electronic Loads are employed in a wide number of applications including electric drives [2], [3], [4], [5], [6], [7], renewables [8], railway [9], microgrids [10], [11], ac grid emulation [12], [13], [14] and energy storage systems [15]. The selection of a specific solution will depend on converter topology, employed filter, and load characteristics. Furthermore, power recirculation (or pump-back) is an important feature for high power applications due to concerns with energy consumption, cooling capability, and grid power availability of the test facilities [3], [16].

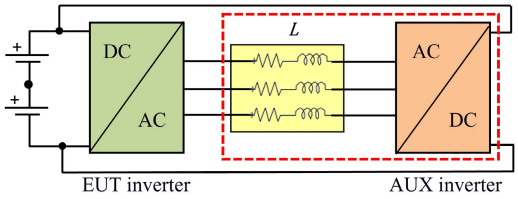

FIGURE 1. ***B2B*** **testbench.**

For the particular case of electric drives, the *AUX* converter emulates the behavior of the electric machine [17]. Controlling the *AUX* converter to make the *EUT* fundamental operating conditions (modulation index, fundamental frequency, fundamental current, power factor) match those expected for the real system is relatively easy to achieve. However, this approach neglects the fact that the harmonic content of the currents for the real system and testbench can significantly differ. Differences in the current harmonics between real system and testbench can have a relevant effect on the loading of power switching devices which can compromise the reliability of the validation process. Furthermore, the emulation results strongly depend on the modulation strategy and the inductors used in the testbench. Changes in the real system might imply a reset of the validation process.

Most testbenches reported in the literature handle power levels in the range of tens of kW [9], [16], [17], [18], [19], while very few are reported for the MW level [3]. In [3], an 11 MW testbench for a variable frequency drive (*VFD*) was reported by GE, neglecting the differences between the testbench and the real system regarding harmonic content or peak currents. At high power levels, it is not feasible to operate *AUX* converter with high switching frequency due to power semiconductor device limitations. This compromises the emulation accuracy since the harmonics injected by the emulation inverter can no longer be neglected. Also, the fact that the *EUT* is often required to operate under different modulation strategies and switching frequencies adds further complexity [20], [21], [22], [23]. Most machine emulators reported in the literature use PWM modulation with switching frequency in the order of tens of kHz [7], [16], [19], [24] where the switching harmonics introduced by the *AUX* inverter are easily filtered since these harmonics have higher frequencies compared to the fundamental component. In those cases, the same fundamental current magnitude can be guaranteed, the harmonic content of the current being less relevant. This is not the case for synchronous modulation techniques used in high-power drives that operate with very low switching-to-fundamental frequency ratios [20], [25] where switching harmonics occur at relatively low frequencies (5th, 7th, 11th, etc.). In these cases, it is not possible to achieve equal current harmonics and at the same time equal current magnitude as will be demonstrated in this paper.

Another challenging aspect that is not properly addressed in the literature, is the selection of the filter inductance coupling the *EUT* and *AUX* inverters (see Fig. 1). In [3], it is indicated that filter inductance should be equal to the machine stator leakage inductance to make the emulation inverter output voltage a direct representation of the machine back emf. However, this approach neglects the effects due to harmonics injected by the *AUX* inverter. In [26], it is recommended that the filter inductance value should be higher than the machine stator transient inductance value in order to compensate for the imposed emulation inverter harmonics and get a comparable THD to the real motor case. A value of 70 μH was selected for a testbench of power in the range of 40 kW, however, it is not indicated on which basis this value was chosen. In the proposed methodology, it is possible to identify the value of the inductance which provides the best matching of harmonic content and/or peak current.

To the best of the author's knowledge, previous works do not consider the influence of both the harmonics injected by the *AUX* inverter and filter selection on the harmonic content or peak current of *EUT* currents. This can result in significant differences with respect to the real application in the operating conditions and stresses of power-switching devices [27], [28]. Instead of trying to precisely reproduce in the testbench the operating conditions of the real system at the fundamental frequency (i.e., same fundamental voltage and current), some degree of freedom could be allowed in the selection of the operating mode of *EUT* and *AUX* converters. This degree of freedom would be used to increase the similarity between the current handled by the *EUT* devices in the testbench and the real system by considering both current harmonics and peak current. Detailed dynamic simulations could be used for this purpose. However, the number of cases that can be evaluated by simulation will be limited, as they are computationally time-consuming. This will compromise the level of optimization that can be achieved using this approach.

This paper proposes a methodology to find the operating point of a testbench which minimizes the differences with respect to a selected operating point of interest in the actual drive. Advantages of the proposed methodology compared to literature are: 1) allowing changes of drive modulation strategy, power topology and testbench filter inductance value. 2) Identifying the best filter inductance value to achieve

the best matching between the real drive and the testbench. 3) Reduced computational efforts since it is based on a simple analytical approach with minimal use of dynamic simulations.

The proposed approach, given an operating point to emulate, consists of three stages: 1) Evaluation of *EUT* and *AUX* inverters operating points and filter inductance values using predefined degrees of freedom, and selection of the optimal solution(s) according to a predefined cost function. Simplified analytical models will be used for this purpose. With the proposed approach, a large number (hundreds of thousands) of operating points and filter inductance values can be evaluated in a few seconds; 2) Verification of the optimal solution(s) by means of detailed dynamic simulations. 3) Implementation in the testbench of the optimal solution(s). The proposed methodology is especially well suited for high-power drives using synchronous modulation methods, though it can be applied to asynchronous PWM/SVM as well. The method can also be applied to any type of AC machine where the main objective is testing the devices in steady-state operation.

It is remarked on the importance of testing passive components (i.e., dc-link capacitors, busbar, etc.) under real system operation conditions. For high-power industrial drives, this process is done separately from the power electronic converter since power recirculation is usually used to decrease consumption and avoid energy waste. In this context, the same methodology proposed in this paper can be applied to test passive components. However, this remains out of the scope of this paper as the main focus is emulating stresses on power-switching devices.

The paper is organized as follows. Real system is described in Section II; testbench description and requirements are addressed in Section III; cost function is defined in Section IV; analytical models used for system emulation are presented in Section V; simulation and experimental results are presented in Sections VI and VII respectively, conclusions being summarized in Section IX.

II. REAL SYSTEM DESCRIPTION

Fig. 2 shows the schematic representation of the two topologies used for the railway traction drive system. Fig. 2a shows a three-level (3L) NPC inverter feeding an induction motor (*IM*), which is a common choice in railway traction drives and Fig. 2b shows a two-level (2L) inverter which will also be discussed in this work. Fig. 3 shows a typical voltage vs. speed profile for traction motors in railway. It is noted that the modulation strategy shown corresponds to a real traction drive. PWM/SVM is used at low speed, while different forms of overmodulation and selective harmonic elimination (*SHE*) techniques are used at medium and high speeds [21], [29], [30]. The reason for this is that railway traction inverter manufacturers are required to comply with the IEC 60349 standard which imposes a limit on the acoustic noise level produced by traction machines [31]. This limit is given as a function of motor speed and therefore, manufacturers use different

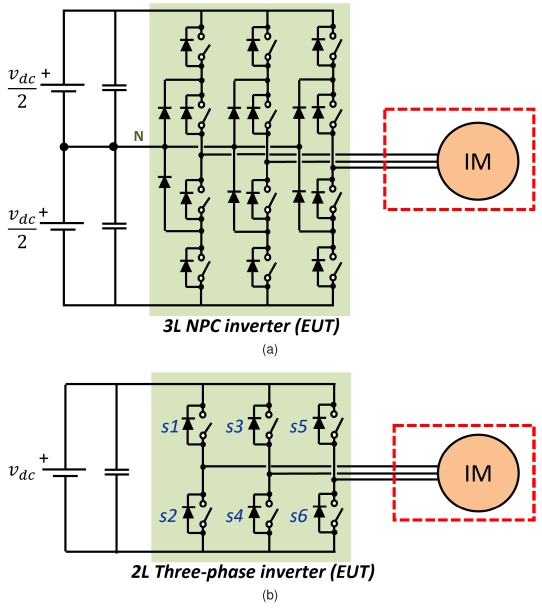

FIGURE 2. Schematic representation of the two topologies used for the railway traction drive, consisting of: (a) 3L NPC inverter (*EUT*) and *IM*, (b) 2L inverter (*EUT*) and *IM*.

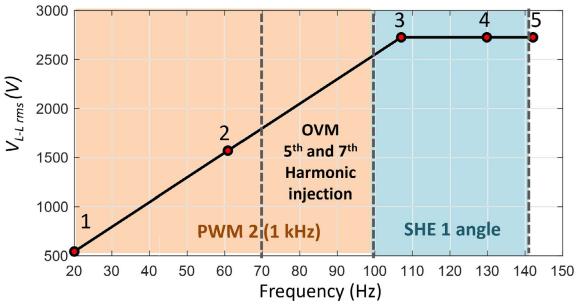

FIGURE 3. *EUT* output voltage and modulation strategy vs. motor speed. Labels 1-5 correspond to selected operating points of the real drive.

modulation strategies along the speed profile. The paper is focused on the high-power operation of traction inverters at high speed where synchronous modulation is used because in this case harmonics injected by the emulation inverter can no longer be neglected which adds further complexity.

The voltage applied by the *EUT* to the *IM* can be represented using complex vector notation as (1):

$$\vec{v}^{EUT} = \frac{2}{3}(v_a^{EUT} + v_b^{EUT} e^{j2\pi/3} + v_c^{EUT} e^{j4\pi/3}) \tag{1}$$

All the following discussion will assume that the system is in steady state. For this case, (1) can be split into fundamental voltage v_f and harmonics v_h (2), with $h = -5, 7, -11, 13, \ldots$ for the usual modulation methods.

$$\vec{v}^{EUT} = \vec{v}_f^{EUT} + \sum_h \vec{v}_h^{EUT} \tag{2}$$

The fundamental voltage $\vec{v}_f^{EUT}$ is defined by both the modulation index M^{EUT} (see Fig. 4) and the fundamental

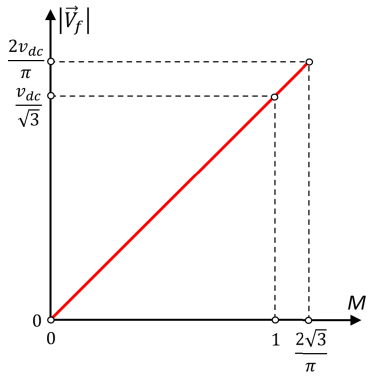

FIGURE 4. Fundamental voltage, $|\vec{V}_f|$ vs. modulation index, M.

frequency $\omega_f t$ (3). It determines the fundamental current, and consequently the fundamental torque and flux levels.

$$\vec{v}_f^{EUT} = \frac{v_{dc}}{\sqrt{3}} M^{EUT} e^{j(w_f t + \alpha^{EUT})} \tag{3}$$

Equation (2) can be represented as a series of the fundamental and harmonic components as in (4), the fundamental voltage being (5).

$$\vec{V}^{EUT} = \left\{ \vec{V}_f^{EUT}, \vec{V}_{-5}^{EUT}, \vec{V}_7^{EUT}, \vec{V}_{-11}^{EUT}, \vec{V}_{13}^{EUT}, \ldots \right\} \tag{4}$$

$$\vec{V}_f^{EUT} = \frac{v_{dc}}{\sqrt{3}} M^{EUT} e^{j\alpha^{EUT}} \tag{5}$$

The harmonic content of *EUT* voltage, $\vec{V}_h^{EUT}$, will depend on the modulation index and modulation strategy. Harmonic components considered in this analysis are $-5, 7, -11$ and 13, but can be easily extended to other harmonics if needed.

Same as the voltages, the resulting currents also consist of a fundamental component and harmonics, as shown by (6) in the frequency domain.

$$\vec{I}^{EUT} = \left\{ \vec{I}_f^{EUT}, \vec{I}_{-5}^{EUT}, \vec{I}_7^{EUT}, \vec{I}_{-11}^{EUT}, \vec{I}_{13}^{EUT}, \ldots \right\} \tag{6}$$

Superposition in steady state will be used for the analysis of (4) and (6). The electric drive in Fig. 2a can be modeled as shown in Fig. 5a. The behavior at the fundamental frequency can be analyzed by means of vector diagrams as shown in Fig. 6. For the sake of simplicity it is assumed that $\alpha^{EUT} = 0$, i.e., $\vec{V}_f^{EUT}$ is aligned with the real axis (see Fig. 6a). This has no effect on the generality of the analysis. The fundamental current $\vec{I}_f^{EUT}$ (see Fig. 6a) will be a function of the fundamental voltage magnitude and frequency, rotor speed (slip) and machine parameters. It can be obtained from the fundamental voltage $\vec{V}_f^{EUT}$ and the back-emf $\vec{V}_{bemf}$, which are connected through the stator transient impedance represented by R_s and L_{ls} (first circuit in the right side of the equality in Fig. 5a).

Current harmonics will depend on the harmonic content of $\vec{V}_h^{EUT}$ and the stator transient inductance,$L_{\sigma s}$, as back-emf harmonics are considered negligible (second circuit in the right side of the equality in Fig. 5a).

III. TESTBENCH DESCRIPTION AND REQUIREMENTS

The *IM* will be replaced by an auxiliary (*AUX*) inverter in the testbench, as shown in Fig. 1. *EUT* and *AUX* inverters are connected back-to-back (*B2B*) through an inductor, power being recirculated through the dc link. The target of the testbench is to accurately reproduce the operating conditions of the *EUT* in the real system in Fig. 2.

Defining the real axis to be aligned with *EUT* inverter fundamental voltage $\vec{V}_f^{EUT\prime}$ (see Fig. 6b), then for the *B2B* testbench:

$$\vec{V}_f^{EUT\prime} = \left|\vec{V}_f^{EUT\prime}\right| e^{j0} \tag{7}$$

$$\vec{V}_f^{AUX} = \left|\vec{V}_f^{AUX}\right| e^{j\alpha^{AUX}} \tag{8}$$

$$\vec{I}_f^{B2B} = \left|\vec{I}_f^{B2B}\right| e^{j\varphi} \tag{9}$$

Superposition will be also used to analyze the behavior of harmonic currents in the testbench. Fig. 5b shows the decomposition of *B2B* into fundamental and harmonic subcircuits. Two subcircuits are needed in this case to account for the harmonics produced by *EUT* and *AUX* inverters.

The following conditions can be established regarding the testbench operation:

1) To achieve the desired fundamental current, *AUX* should produce a fundamental voltage given by (10), with ω_f being the fundamental frequency and L the testbench filter inductance. It is noted that since the proposed method is intended for high values of the ω_f (*SHE* region in Fig. 3), filter resistance R can be safely neglected.

$$\vec{V}_f^{AUX} = \vec{V}_f^{EUT\prime} - j\omega_f L \vec{I}_f^{EUT} \tag{10}$$

2) To match the harmonic content of the currents of testbench (I_h^{B2B}) and real system (I_h^{EUT}), the *AUX* inverter should inject the voltage harmonics required to compensate for the different values of the inductance of machine $L_{\sigma s}$ and testbench L (resistances being neglected in this case); (11) holds in this case.

$$\vec{V}_h^{AUX} = \vec{V}_h^{EUT\prime} \frac{(L_{\sigma s} - L)}{L} \tag{11}$$

3) The *AUX* inverter should not produce frequency components at frequencies different from those produced by *EUT* (or should be negligible). Unwanted current harmonics would circulate through *EUT* inverter otherwise, modifying its electrical and thermal behavior.

All these conditions could be achieved by operating the *AUX* inverter using PWM with a high switching frequency. In this case, the voltage commanded to the *AUX* inverter would include the fundamental and harmonic voltages needed to achieve the desired currents. Voltage harmonics due to the *AUX* inverter would be filtered off by the testbench inductance L, provided that its switching frequency is high enough. While this approach might be feasible for low power systems, it is not viable in general for high power converters, as thermal limits make unfeasible the use of high switching frequencies for *AUX* inverters.

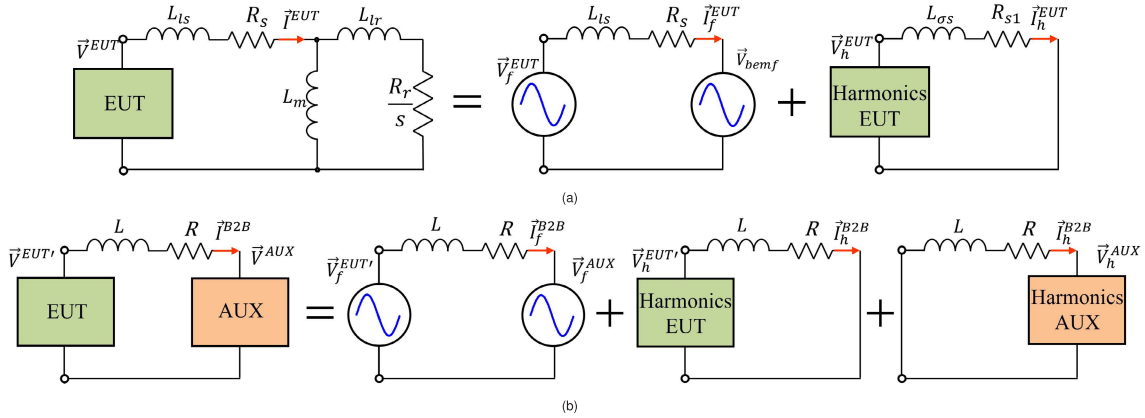

FIGURE 5. Decomposition of system circuits using superposition (a) *EUT* inverter and *IM*, (b) *B2B* connection of *EUT* and *AUX* inverters. L_m, L_{ls} and L_{lr} are the magnetizing and leakage inductances, R_s and R_r are the resistances, s is the slip, R_{s1} and $L_{\sigma s}$ are the stator transient resistance and inductance, L is testbench filter inductance, R is parasitic resistance of L. Variables denoted by prime in (b) refer to testbench parameters.

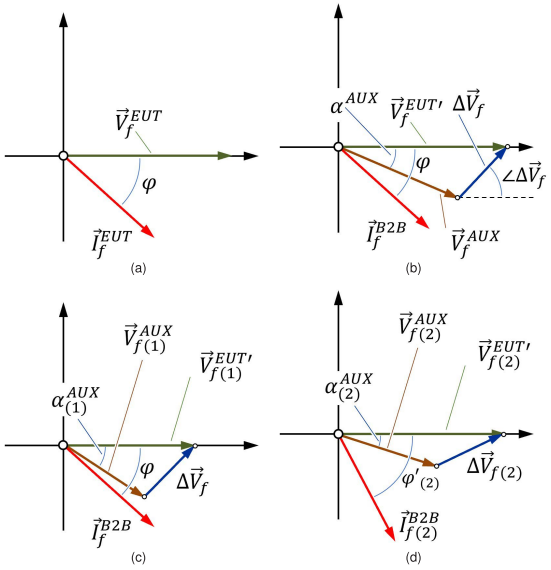

FIGURE 6. Vector diagrams at fundamental frequency. $|\Delta\vec{V}_f|$ and $|\vec{I}_f^{B2B}|$ remain invariant in all cases. a) Real system (*EUT*+*IM*); b)-d) *B2B* testbench; b) same $\vec{V}_f^{EUT}$ and power angle φ as for a); c) $\vec{V}_f^{EUT}$ varied, φ, I_f^{B2B} invariant; d) φ varied.

It is concluded from the preceding discussion that the voltage produced by the *AUX* inverter in Fig. 1 can be modeled as (12) and (13) (see Fig. 6b-6d).

$$\vec{V}^{AUX} = \left\{ \vec{V}_f^{AUX}, \vec{V}_{-5}^{AUX}, \vec{V}_7^{AUX}, \vec{V}_{-11}^{AUX}, \dots \right\} \tag{12}$$

$$\vec{V}_f^{AUX} = \frac{v_{dc}}{\sqrt{3}} M^{AUX} e^{j\alpha^{AUX}} \tag{13}$$

Same as for the *EUT*, voltage harmonics will be a function of the modulation index and modulation strategy. The resulting current will be of the form shown in (14); the condition to exactly reproduce in the testbench the operating conditions of the real system would be (15).

$$\vec{I}^{B2B} = \left\{ \vec{I}_f^{B2B}, \vec{I}_{-5}^{B2B}, \vec{I}_7^{B2B}, \vec{I}_{-11}^{B2B}, \dots \right\} \tag{14}$$

$$\vec{I}^{B2B} = \vec{I}^{EUT} \tag{15}$$

Under the premise that *AUX* inverters cannot switch significantly faster than *EUT* inverters, condition 1) is easily achieved by proper selection of M^{AUX} and α^{AUX} in (13). Condition 3) is achieved by using a modulation strategy in the *AUX* inverter which produces harmonics at the same frequencies as *EUT*. However, the voltage harmonics injected by the *AUX* inverter will not comply in general with (11), meaning that condition 2), and consequently (15), will not be satisfied.

IV. COST FUNCTION DEFINITION

It is concluded from the previous discussion that it is not possible to achieve in the testbench both the same fundamental and harmonic currents of the real system. A cost function C (16) can be used to objectively assess the level of similarity between the testbench and the real system.

$$C = \sum_{h=1}^{N} \gamma_h \frac{\left(\left|I_h^{EUT} - I_h^{B2B}\right|\right)^2}{(I_h^{EUT})^2} + \gamma_\varphi \frac{(\varphi - \varphi\prime)^2}{\varphi^2} + \gamma_M \frac{\left(M^{EUT} - M^{EUT\prime}\right)^2}{(M^{EUT})^2} \tag{16}$$

γ_h, γ_φ and γ_M being the weighting factors of current harmonic components, power factor and modulation index respectively. Selection of these weighting factors is done according to the priorities and concerns of each application (values for analyzed cases being shown in Table 3).

The objective is to select the operating point of *EUT* and *AUX* inverters which minimizes C. Constraints and targets used to define C are the following:

- Fundamental current magnitude and fundamental frequency will be forced to be the same for the real

system and the testbench (17). Consequently, they are not included in the cost function.

$$\left|\vec{I}_f^{B2B}\right| = \left|\vec{I}_f^{EUT}\right| \tag{17}$$

Solutions for (17) can be easily found from the vector diagram in Fig. 6. Known the desired fundamental current and the inductance L connecting *EUT* and *AUX* inverters, the required differential voltage magnitude is obtained by (18).

$$\left|\Delta\vec{V}_f\right| = \omega_f L \left|\vec{I}_f^{B2B}\right| \tag{18}$$

- Differences (errors) between current harmonics of the real system and the testbench should be minimized. For this purpose, they will be included in the cost function (16) (first term on the right side), γ_h being the applied weight coefficient. In this analysis, each harmonic component is assigned a weight coefficient inversely proportional to its order (i.e., the lower the harmonic the more weight it has in the cost function). This criterion can be changed depending on the objective of the analysis.
- With the aim of reducing the error in the harmonic content of the current, differences in the modulation index of *EUT* and power factor φ between the testbench and the real system are allowed. Such differences will be considered in the cost function (16) (second and third terms on the right side), with γ_φ and γ_M being the corresponding weighting coefficients. Fig. 6b, 6c, 6d show three different operating points of *EUT* and *AUX* inverters. In all the cases (19) holds, and consequently the fundamental current (17) remains invariant.

$$\left|\vec{V}_f^{EUT\prime} - \vec{V}_f^{AUX}\right| = \left|\Delta\vec{V}_f\right| \tag{19}$$

- The modulation method of the *EUT* inverter must be the same for the real system and the testbench. On the contrary, for the *AUX* inverter, different synchronous modulation methods can be used aimed to minimize the error in the current harmonics.

The most straightforward strategy to implement the described approach is to run a large number of dynamic simulations of the system in Fig. 1, varying $\vec{V}_f^{EUT\prime}$, $\Delta\vec{V}_f$, and the modulation strategy of the *AUX* inverter, to find the configuration (i.e., operating point) which minimizes (16). However, dynamic simulations are computationally time-consuming, which limits the number of cases that can be analyzed in practice. Furthermore, changes in the machine design, operating point (e.g. frequency), testbench inductance, *EUT* modulation strategy, etc., would require a new set of simulations, often requiring starting over.

Minimization of (16) using analytical methods is discussed in the next section. The proposed approach requires knowledge of the voltage harmonic content injected by the *EUT* and *AUX* inverters, which will depend on the modulation strategy and modulation index. This data is obtained during a commissioning process and has an associated computational burden. However, once the data is stored, evaluation of (16) will not require time consuming dynamic simulations but fast analytical calculations. Due to this, hundreds of thousands of operating conditions can be evaluated in seconds.

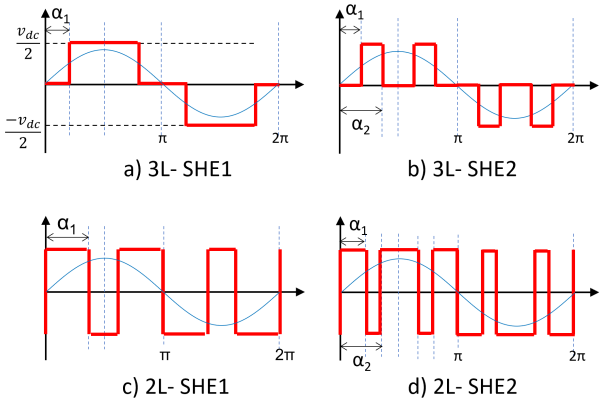

FIGURE 7. Phase voltages using *SHE1* and *SHE2* for the case of 3L and 2L inverters.

V. SYSTEM EMULATION USING ANALYTICAL FUNCTIONS

If the harmonic content of the voltage being applied by *EUT* and *AUX* inverters is known, the resulting current harmonics can be obtained for different values of h by using (20).

$$\vec{I}_h^{B2B} = \frac{\Delta\vec{V}_h}{jh\,\omega_f L} = \frac{\vec{V}_h^{EUT\prime} - \vec{V}_h^{AUX}}{jh\,\omega_f L} \tag{20}$$

Two cases can be distinguished:

1) For asynchronous PWM/SVM methods, the harmonic content will depend on the modulation index, fundamental frequency and switching frequency. Intermodulation harmonics will occur in this case. These harmonics can be especially harmful and difficult to model when switching and fundamental frequencies are relatively close to each other.
2) For synchronous modulation methods, the harmonic content is only a function of the modulation index, which significantly eases the analysis. Interestingly, operation with synchronous modulation and low-switching frequency is the most difficult to reproduce in the testbench.

Synchronous modulation methods will be the target of the analysis presented following. Two different modulation strategies will be considered to exemplify the process: *SHE* with one angle (*SHE1*) and two angles (*SHE2*) [32], [33]. The phase voltage waveforms for these modulation techniques are shown in Fig. 7.

A. VOLTAGE HARMONICS FOR THE 3L AND 2L INVERTERS

Fig. 8 shows the magnitude of the complex vector harmonic components of the output voltage vs. modulation index for the 3L inverter in Fig. 2a using *SHE1*. For all the figures shown in this section, voltage is given in per unit (p.u.) of $\frac{2v_{dc}}{\pi}$. Each spectrum was obtained from a dynamic simulation using

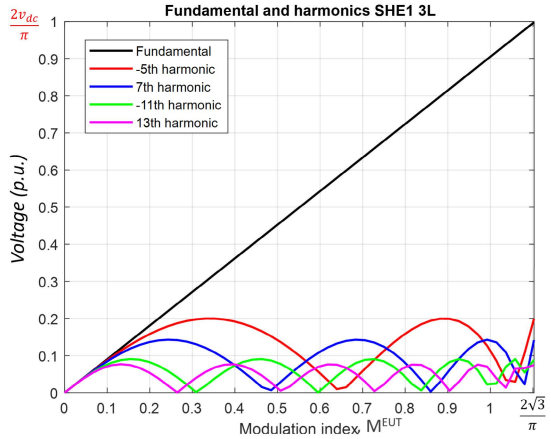

FIGURE 8. Fundamental and harmonic content of the voltage vs. modulation index M^{EUT} of a 3L inverter using *SHE1*.

Simulink to model the inverter considering real power switching device model as well as including dead-time. 51 modulation indices were simulated in total. Simulation of one full cycle of the fundamental voltage is enough for this purpose (0.2s at 1μs time step). In the stationary reference frame, the frequency spectrum includes the 1^{st} (fundamental), -5^{th}, 7^{th}, -11^{th}, 13^{th}, ... In this paper, only the fundamental and harmonics -5^{th}, 7^{th}, -11^{th} and 13^{th} will be considered. Therefore, the information in Fig. 8 can be stored in a 51 x 5 complex vector look-up table (*LUT*), each element being of the form given by (21).

$$\vec{V}_h^{EUT} = |\vec{V}_h^{EUT}|e^{j\angle\vec{V}_h^{EUT}} \tag{21}$$

The same process can be followed for the case of a 3L inverter using *SHE2*. The frequency spectrum of the voltage will include the same harmonics as in Fig. 8. However, they will be a function of modulation index and first commutation angle α_1. In is noted that the second commutation angle of *SHE2* α_2 is not an independent variable, but depends on modulation index and α_1 as shown by (22) [33]. Therefore, each voltage harmonic injected by the inverter must be stored now in a two-dimensional *LUT*, as shown in Fig. 9.

$$cos(\alpha_1) - cos(\alpha_2) = \frac{\pi}{4}M^{EUT} \tag{22}$$

The same process can be followed for a 2L inverter in Fig. 2b. Fig. 10 shows the magnitude of the harmonics vs. modulation index when using *SHE1* (see Fig. 7-c). Fig. 11 shows the magnitude of the harmonics vs. modulation index and angle α_1 when using *SHE2* (see Fig. 7-d). The relation between the two commutation angles, α_1 and α_2 is given by (23).

$$1 - 2\,cos(\alpha_1) + 2\,cos(\alpha_2) = \frac{\pi}{4}M^{EUT} \tag{23}$$

B. MINIMIZATION OF COST FUNCTION

Once the harmonic content of the modulation strategies being considered has been obtained and stored, the optimization

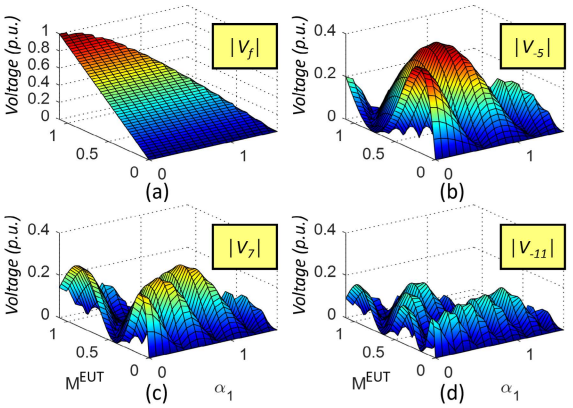

FIGURE 9. a) Fundamental and b)-d) harmonic content of the voltage vs. modulation index M^{EUT} and angle α_1 of a 3L inverter using *SHE2*.

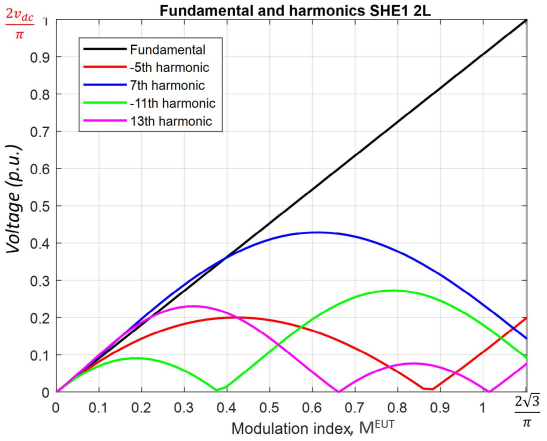

FIGURE 10. Fundamental and harmonic content of the voltage vs. modulation index M^{EUT} of a 2L inverter using *SHE1*.

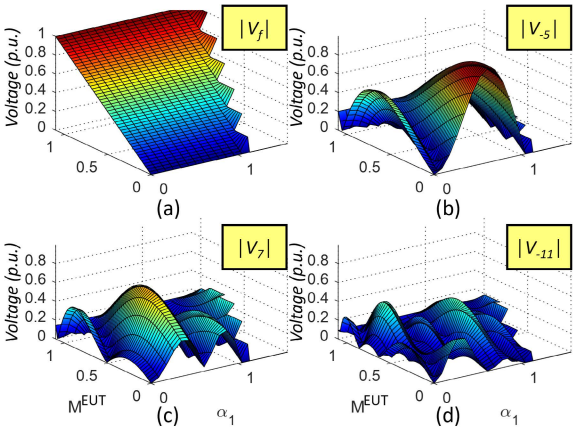

FIGURE 11. a) Fundamental and b)-d) harmonic content of the voltage vs. modulation index M^{EUT} and angle α_1 of a 2L inverter using *SHE2*.

process is as follows (encircled number refers to the stages shown in Fig. 12):

① Once the desired operating point of *EUT+IM* is selected, this will determine *EUT* modulation index M^{EUT} and fundamental frequency ω_f, as well as motor speed.

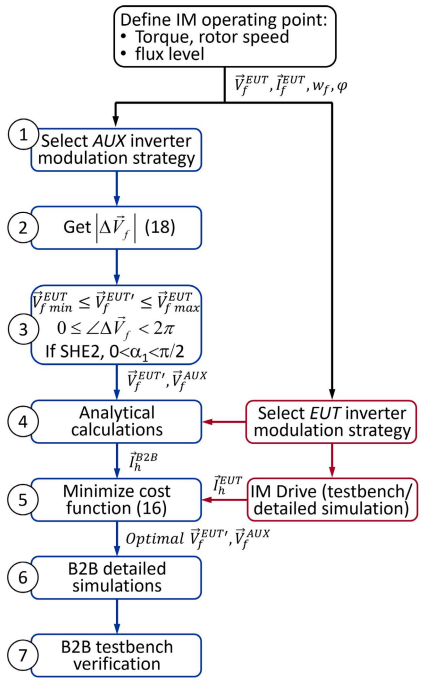

FIGURE 12. Overview of the optimization process.

Modulation strategy of *EUT* is also defined at this stage and will remain invariant. Fundamental current $\vec{I}_f^{EUT}$ and harmonic current content $\vec{I}_h^{EUT}$ of *EUT* can be obtained either by means of simulation, or in the real drive system if available.

② The voltage $\left|\Delta\vec{V}_f\right|$ required to achieve the desired fundamental current $\left|\vec{I}_f^{EUT}\right|$ is obtained using (18) and will remain invariant for the remaining steps.

③ Optimization starts at this point. *EUT* fundamental voltage $\vec{V}_f^{EUT\prime}$ and angle of the differential voltage $\angle\Delta\vec{V}_f$ applied to the inductor are varied within the limits indicated in Fig. 12. It is noted that the limits for $\angle\Delta\vec{V}_f$ vary according to $\vec{V}_f^{EUT\prime}$ and the used filter inductance value (see (18), (19)). The *AUX* inverter voltage is obtained as (24), its phase angle being (25). The power angle φ (see Fig. 6) is obtained using (7), (9).

$$\vec{V}_f^{AUX} = \vec{V}_f^{EUT\prime} - \Delta\vec{V}_f \tag{24}$$

$$\alpha^{AUX} = \angle\vec{V}_f^{AUX} \tag{25}$$

④ The modulation method for *EUT* is constrained to be the same as for the real system. On the contrary, different modulation methods can be evaluated for the *AUX* inverter aimed to minimize the error in the current harmonic contents (first term on the right side of the cost function in (16)). Voltage harmonics $\vec{V}_h^{EUT\prime}$ and $\vec{V}_h^{AUX}$ injected by *EUT* and *AUX* inverters are obtained from the corresponding *LUTs* (Fig. 8 to Fig. 11) as described in Section V-A. Once $M^{EUT\prime}$, M^{AUX} and α^{AUX} are known, it is straightforward to obtain the harmonic content of *EUT* and *AUX* output voltage. The resulting current harmonics are easily obtained using (26).

$$\vec{I}_h^{B2B} = \frac{\vec{V}_h^{EUT\prime} - \vec{V}_h^{AUX} e^{j\alpha_h^{AUX}}}{j\,h\,\omega_f\,L} \tag{26}$$

It is noted that the harmonic h of the *AUX* inverter read from *LUTs* must be rotated as shown by (27).

$$\alpha_h^{AUX} = h\,\alpha^{AUX} \tag{27}$$

⑤ For each $\left(\vec{V}_f^{EUT\prime}, \angle\Delta\vec{V}_f\right)$ set, the cost function C is obtained using (16). The weighting factors are calculated using (28), (29). According to the selected criteria for this analysis, the current harmonic components are assigned weights inversely proportional to the harmonic order, giving the fifth component the highest weight where the total weight is one. The minimum computed value of the cost function defines the operating point of the *B2B* which provides the best agreement with the real system *EUT+IM*.

$$\sum_{h=-5,7,-11,13} \gamma_h + \gamma_\varphi + \gamma_M = 1 \tag{28}$$

$$\gamma_{-5} = \frac{7}{5}\gamma_7 = \frac{11}{5}\gamma_{-11} = \frac{13}{5}\gamma_{13} \tag{29}$$

⑥ The obtained optimal *B2B* operating point is simulated using a detailed Simulink model. Current harmonics are compared to the analytically predicted values to verify the analytical calculations.

⑦ Finally, the selected *B2B* operating point can be used for the experimental verification of the *EUT* in the testbench.

VI. SIMULATION RESULTS

This section shows some examples of the application of the proposed methodology. *EUT* and *IM* parameters of the real traction drive, and values of inductor L available for the *B2B* configuration in the full-scale testbench are provided in Table 1. Using these parameters, detailed simulation models are developed using MATLAB/Simulink to precisely model the real motor and drive. It is remarked that the *B2B* configuration is totally reversible providing functionality in the four machine quadrants. Results are shown for forward motor quadrant only since reverse motoring would not show any difference in current harmonic content. In this case, current and voltage vectors would have the same magnitude and phase but with opposite direction. Selected operating point for the *EUT+IM* system is given in Table 2 in forward motor and generator modes of operation. The resulting current wave

TABLE 1. System parameters.

IM	
Rated values	$V_{nom} = 2727$ kV, $I_{nom} = 268$ A, $P_{nom} = 1084$ kW
Parameters	$L_m = 25.6$ mH, $L_{ls} = 0.824$ mH, $L_{lr} = 0.6827$ mH
EUT	
Dc link	3.6 kV
Modulation	*SHE1*, *SHE2*
Available testbench inductors (mH)	
0.89, 1.426, 1.782, 3.564, 7.13, 8.912	

TABLE 2. *IM* operating point.

	Motor	Generator
Fundamental voltage, $\vec{V}_f^{EUT}$	1466.5 V	1434.6 V
Modulation index, M^{EUT}	0.8147	0.797
Fundamental current, $\vec{I}_f^{EUT}$	246 A	246 A
Fundamental frequency, ω_e	672.3 rad/s (107 Hz)	672.3 rad/s
Rotor speed, ω_r	668.9 rad/s (106.465 Hz)	675.7 rad/s
Power angle, φ	28°	152°

TABLE 3. *EUT* and *AUX* inverters modulation and cost function weights.

Case	Modulation	γ_{-5}	γ_7	γ_{-11}	γ_{13}	γ_M	γ_φ
(A)[1]	*SHE1 & SHE1*	0.195	0.140	0.09	0.075	0.25	0.25
(B)[2]	*SHE1 & SHE1*	0.392	0.28	0.178	0.15	0.0	0.0
(C)[2]	*SHE1 & SHE2*	0.392	0.28	0.178	0.15	0.0	0.0
(D)[2]	*SHE2 & SHE2*	0.392	0.28	0.178	0.15	0.0	0.0

[1] Only magnitude of current harmonics being considered.
[2] Magnitude and phase of current harmonics being considered.

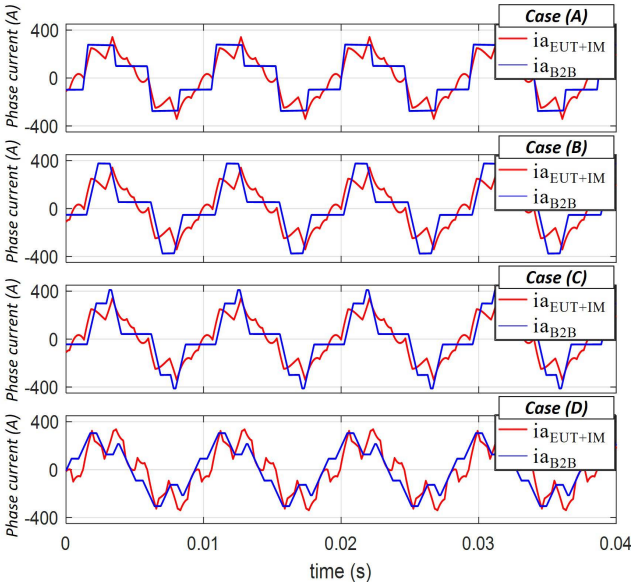

FIGURE 13. Simulation results. *EUT+IM* (red) and *B2B* (blue) i_a current. *IM* operating conditions are given in Table 1. Modulation strategies for *EUT* and *AUX* inverters and cost function weights for (A) - (D) cases are shown in Table 3.

shape obtained by means of dynamic simulation is shown in Fig. 13 (red trace) for the forward motor mode. Results for forward generator case are not included in the paper since it has similar current harmonic content compared to the forward motor case.

Fig. 14 shows the relevant variables for the *B2B* configuration obtained using (24)-(27). Active and reactive powers, and the considered current harmonics were obtained as a function of $\vec{V}_f^{EUT\prime}$ and $\angle\Delta\vec{V}_f$. In all cases, $|\Delta\vec{V}_f|$, and consequently the fundamental current, remained constant. It is noted that control in *EUT+IM* as well as in *B2B* testbench is done in open loop since the target is to test the converter in steady-state operation. This enables the use of simple analytical calculations to obtain the *B2B* set point which results in the least mismatch in current harmonics between real system (*EUT+IM*) and *B2B* testbench.

The coefficients selected for the calculation of the cost function are shown in Table 3-*Case A*. Note that only the magnitude of current harmonics was considered. The cost function results for the value of the inductance L in Fig. 14 are shown in Fig. 15c).

A sweep of the filter inductance value was performed in order to assess its impact on the cost function. This approach can be used to select the most adequate value of inductance for a given operating point. Fig. 15 shows the cost function C results for the available values of inductor L. Fig. 16 shows the optimum of the cost function for each value of L in the (M^{EUT}, $\angle\Delta\vec{V}_f$) plane. Fig. 17-*Case (A)* (red trace) shows the optimal cost function value in terms of L, the minimum occurring for $L = 1.782$ mH.

To verify the results of the optimization process, the phase current for the optimal *B2B* operating point was obtained by means of dynamic simulation. Currents for the *EUT+IM* and *B2B* are shown in Fig. 13-*Case (A)*. The cost function obtained using dynamic simulation results showed an excellent agreement with the value from the analytical approach. It is interesting to note that regardless of the small value of the cost function, differences between the currents for *EUT+IM* and *B2B* cases in Fig. 13-*Case (A)* are relevant. The reason for this is that only current harmonics magnitude was considered to obtain C, phase angles were disregarded. A result of this is that the peak current for *B2B* case is significantly smaller than peak current for *EUT+IM* case, as shown in Fig. 18 (traces in red).

Optimization process was repeated considering both magnitude and phase of current harmonics using the weight coefficients in Table 3-*Case (B)*. Modulation index and power factor are disregarded in this case. Traces in blue in Fig. 17 and Fig. 18 show C_{min} and peak current for the different values of L. The lowest value of C_{min} occurs for $L = 3.564$ mH, but it is significantly larger compared to *Case (A)*. Fig. 13-*Case (B)* shows the current for the *B2B* obtained by means of a dynamic simulation. Differences between *EUT+IM* and *B2B* cases are still relevant.

To improve the similarity between *EUT+IM* and *B2B* cases, *SHE2* was used with *AUX* inverter [*Case (C)* in Table 3]. It is noted that this implies higher switching losses in *AUX* inverter. Fig. 17 and Fig. 18 (magenta trace) shows C_{min} and peak current vs. L, the minimum of C_{min} occurring for $L = 3.564$ mH. Fig. 13-*Case (C)* shows the current for *EUT+IM* and *B2B* configurations at C_{min}, a slight improvement being observed with respect to *Cases (A)* and *(B)*.

Finally, results when *SHE2* is used in *EUT+IM* system are shown in Fig. 13, Fig. 17 and Fig. 18 (black trace) respectively. Weight coefficients are shown in Table 3-*Case (D)*. C_{min} as well as the smallest error in the peak current are now obtained for $L = 7.13$ mH [point(5)]. Consistently with these results, a better agreement between current waveform of *EUT+IM* and *B2B* is observed in this case in Fig.13.

It is interesting to see that the points with the best peak current matching (i.e., points(1) and (2) Fig.18) have the worst harmonic content matching (Fig.17) while the optimal

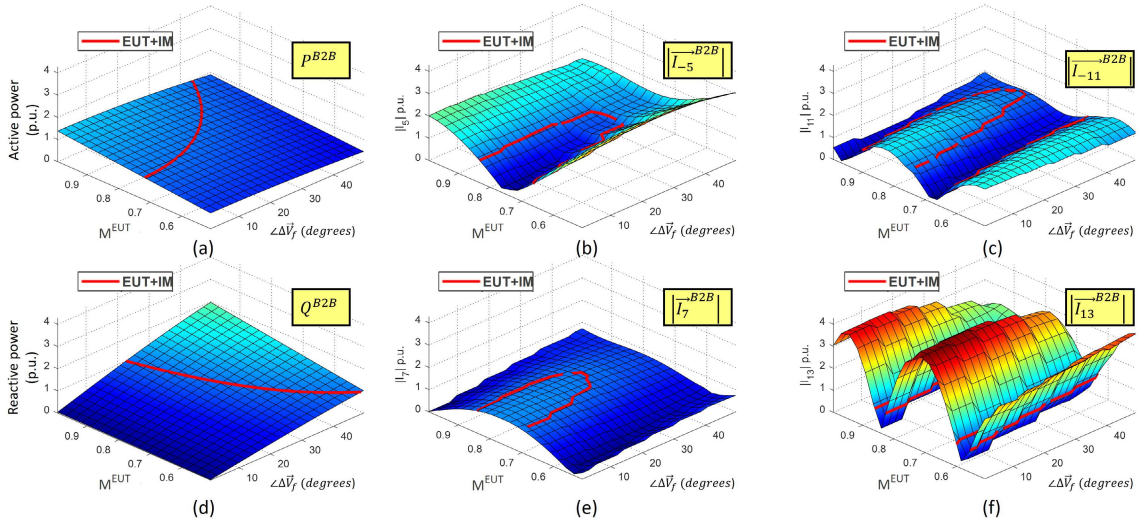

FIGURE 14. Variation with modulation index and angle of a) active power, d) reactive power, and b) -5^{th}, e) 7^{th}, c) -11^{th} and f) 13^{th} of current vector harmonics. Magnitude of the fundamental current remained constant. *B2B* inductor $L = 1.782$ mH. *SHE1* modulation is used for both *EUT* and *AUX*. The red line indicates the value of each variable for the *EUT+IM* case.

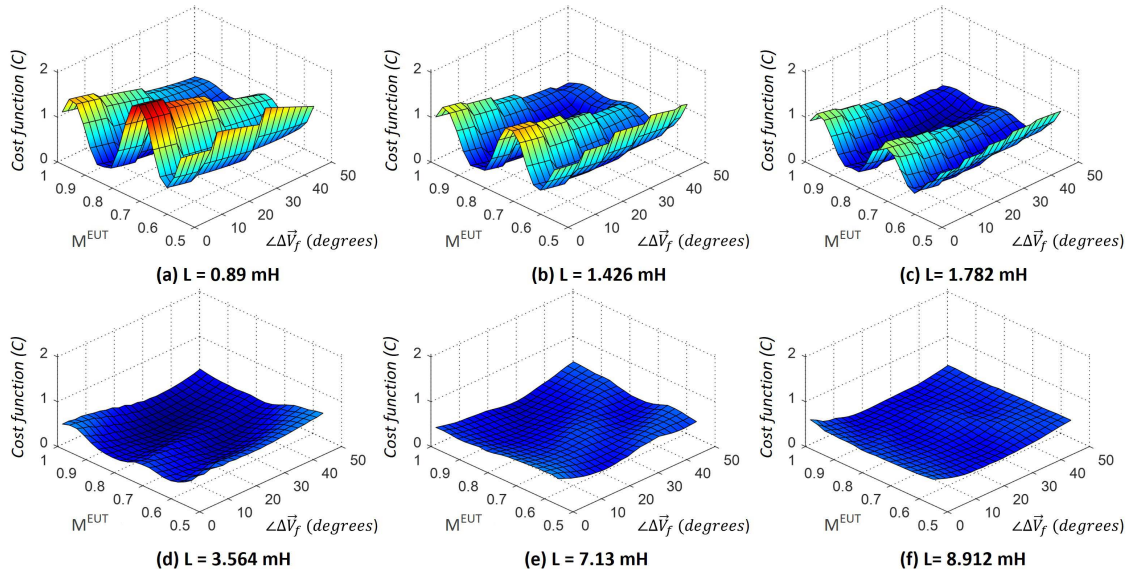

FIGURE 15. Cost function *C* vs. modulation index and angle for the inductances available in the testbench. Magnitude of the fundamental current remains constant. Modulation strategies and weight factors correspond to *Case (A)* in Table 3.

point (point(5) at C_{min}) has the best harmonic matching with a relatively small difference in peak current value of 9%. It is also noted that weight factors for cases *Case (B)*-to-*(D)* were chosen to minimize the error in the harmonic content of the currents, and power angle φ was disregarded for the cost function. Differences in the power angle of *EUT+IM* and *B2B* will result in differences in the conduction time of IGBTs and diodes, and consequently in the losses distribution. It is concluded that weight factors allow customizing the optimization process according to the importance given to harmonic current content, peak current, conduction times of IGBTs and diodes, etc., but their selection should be analyzed carefully.

It is finally remarked that for the results shown in this section, a total number of 470, 304 configurations have been analyzed, with a time consumption of $\approx$ 48 s in a regular computer (Intel i7-4770, 3.40 GHz, 10 GB RAM). The time required to run this number of dynamic simulations would be $\approx$ 5 years with the same hardware. Only four dynamic simulations have been required.

VII. EXPERIMENTAL VERIFICATION

A *B2B* scaled-down testbench following the schematic diagram of Fig. 19 was developed as shown in Fig. 20. The characteristics of the testbench are shown in Table 4. It is

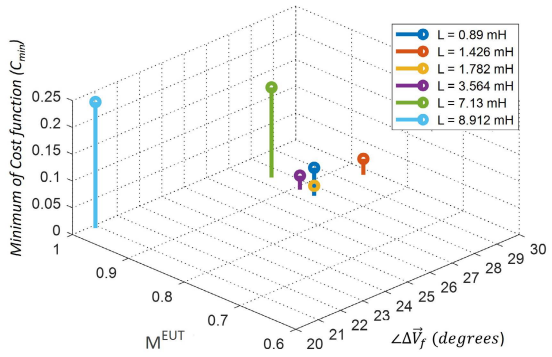

FIGURE 16. Minimum value of the cost function C_{min} for the six cases shown in Fig. 15.

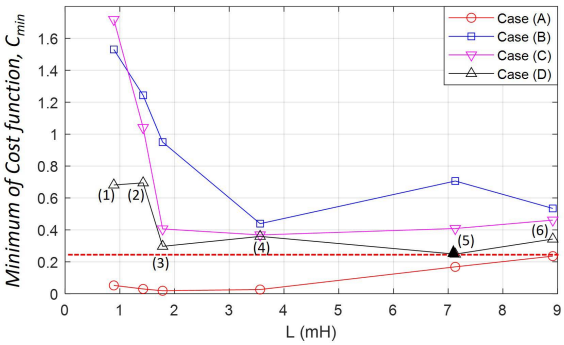

FIGURE 17. Analytical results: C_{min} vs. inductor L for cases (A, B, C, D) in Table 3.

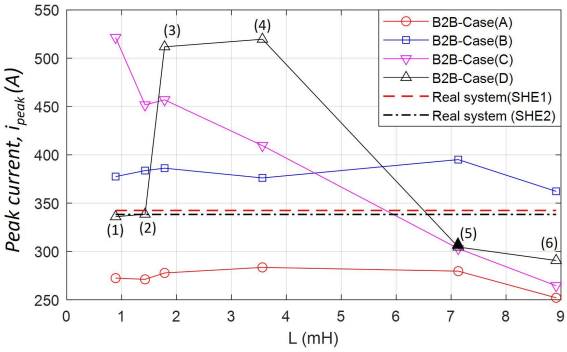

FIGURE 18. Dynamic simulation results: peak value of phase current, i_a, in the testbench (*B2B*) and in the real system (*EUT+IM*) vs. inductor L for cases (A, B, C, D) in Table 3.

noted that a full-rated testbench for the final application is being constructed by Ingeteam Power Technology.

The real drive is developed following the schematic diagram of Fig. 2b. The parameters of the *IM* used for the experiments are given in Table 4. The operating point given in Table 5 was selected as an example. The resulting experimental waveforms of the real drive, *EUT+IM*, are shown in Fig. 21.

As concluded from the simulations shown in the previous section, the best agreement between the *EUT+IM* and *B2B* when the *EUT* inverter uses *SHE2* modulation is achieved when *AUX* inverter also uses *SHE2*. The equivalent

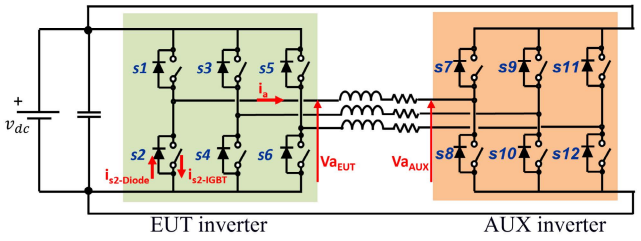

FIGURE 19. *B2B* testbench schematic.

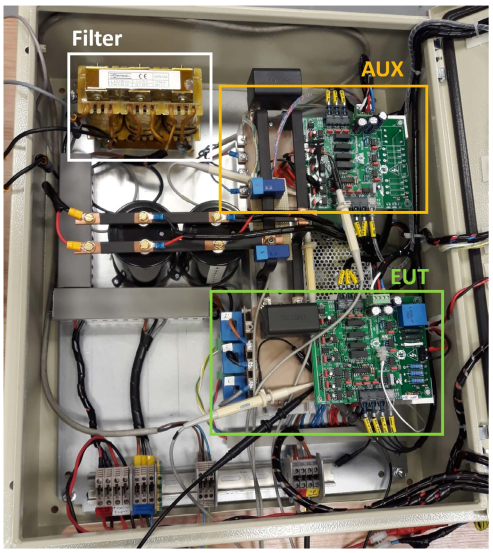

FIGURE 20. *B2B* testbench prototype.

TABLE 4. Experimental *B2B* testbench and *IM* parameters.

IM	
Number of poles	4
Nominal Voltage	400 V
Frequency	50 Hz
Nominal speed	1425 r/min
Rated Power	1.1 kW
***B2B* testbench**	
Topology	2L three-phase inverters
Rated dc-link voltage	400 V
Rated power	5 kW
Switching devices	Three-phase IGBT module Fuji Electric $-7MBP50VDA060-50$
Filter	1.8 mH

TABLE 5. Experimental results: *EUT+IM* operating point.

Fundamental voltage	$\vec{V}_f^{EUT} = 208.68$ V
Modulation strategy	*SHE2*
Modulation index	$M^{EUT} = 1.0414$
Fundamental current	$\vec{I}_f^{EUT} = 1.8876$ A
Fundamental frequency	$\omega_e = 628.3$ rad/s (100 Hz)
Power angle	$\varphi = 28.45°$

switching frequency being 1 kHz since, in *SHE2*, there are 10 transitions per cycle of the fundamental frequency (i.e., 100 Hz). Having defined the *EUT+IM* operating point and *AUX* modulation strategy, the proposed optimization process

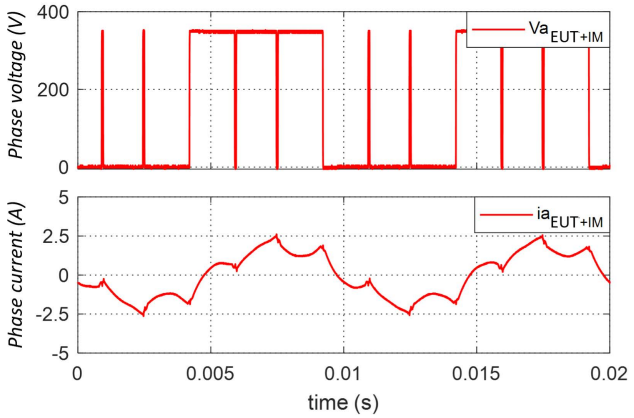

FIGURE 21. Experimental results for *EUT+IM* at the selected operating point showing phase voltage (v_a) and phase current (i_a) (see schematic in Fig. 2b).

TABLE 6. Experimental results. Optimal *B2B* testbench operating point.

	EUT	*AUX*
Modulation index	$M^{EUT} = 0.796313$	$M^{AUX} = 0.774$
SHE2 angles	$\alpha_1^{EUT} = 1.04719$ $\alpha_2^{EUT} = 1.20136$	$\alpha_1^{AUX} = 1.04719$ $\alpha_s^{AUX} = 1.21218$
Power angle	$\varphi = 80°$	
Cost function	C_{min} = 0.90711	

can be carried out as described in Fig. 12. Both magnitude and phase of current harmonics are considered using the weight coefficients shown in Table 3-*Case (D)*. Magnitude of the fundamental current remained constant and equal to that of the *EUT+IM* at the selected operating point (see Table 5). The predicted optimal *B2B* operating point (i.e., C_{min}) is shown in Table 6.

Fig. 22 shows the experimental results of the *B2B* optimal operating point compared with the dynamic simulation results. Phase voltages for both *EUT* and *AUX* are shown as well as phase current compared with the *EUT+IM* real drive current. It is noted that the difference between phase voltages of *EUT* and *AUX* is small (see Table 6 and Fig. 22). This is due to the low voltage required in the coupling filter inductance to transfer the required current. This agrees with the simplified circuit shown in Fig. 5a, where *EUT* and *bemf* voltages are close to each other, and only a small voltage drop occurs at the impedance connecting both.

The difference seen in the instantaneous current waveform between the *B2B* and the real drive *EUT+IM* can be understood by comparing the magnitude and phase of each harmonic component in both cases. Fig. 23 shows the magnitude of the current harmonics for the different cases. It can be observed that the magnitude of the fundamental current remained constant in all cases. Also, it can be seen that the predicted analytical calculation (magenta) has a good matching to the experimental (green) and simulation (blue) results. It is observed that there is a significant decrease of the -5^{th} for the *B2B* with respect to the *EUT+IM* case, while 7^{th} and -11^{th} have increased. This is a consequence of having established an exact match of fundamental current

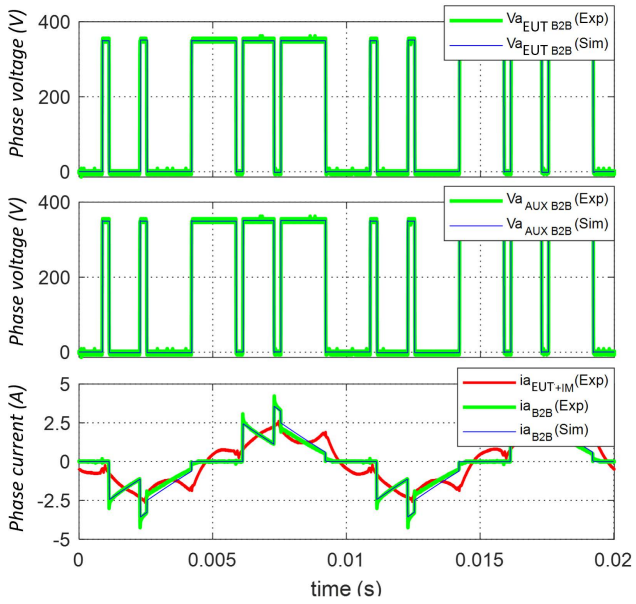

FIGURE 22. Experimental vs. simulation results for the *B2B* showing *EUT* and *AUX* phase voltages (v_a) and phase current (i_a) (see schematic in Fig. 19).

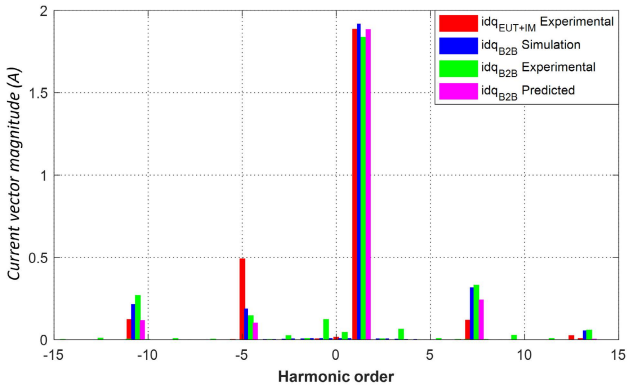

FIGURE 23. Magnitude of the frequency spectrum of the current vector for *EUT+IM* and *B2B* (dynamic simulation, experimental and analytical prediction).

as a premise. Better matching of current harmonics could be achieved if the condition in (17) is removed, i.e., error of the fundamental current is included in the cost function. Changes to the cost function can be applied to better suit specific requirements of the application of interest. It is noted that the frequency resolution obtained in the FFT analysis is 50 Hz and the Nyquist frequency is 500 kHz (sampling rate of 1 MS/s), which are enough to capture the fundamental frequency used in the paper (100 Hz), and the harmonic components considered (-5, 7, -11, and 13), and avoiding the risk of aliasing.

Finally, it is worth remarking that, for the testbench in a *B2B* configuration, a startup procedure is necessary to avoid undesired transients which may jeopardize the devices. In this case, a startup process is implemented based on ramping the commanded modulation indices as well as the angle between

the fundamental voltage components of both *EUT* and *AUX* inverters, α^{AUX}.

VIII. CONCLUSION

A methodology to find the operating conditions of a test-bench to reproduce with the highest possible accuracy the behavior of the actual system has been proposed. The method uses simple analytical functions, enabling the evaluation of hundreds of thousands of testbench operating points in a few seconds. A cost function is used to customize the optimization to the specific priorities of each application. The proposed methodology is especially well suited for power converters using synchronous modulation methods operating with low switching frequencies, i.e., with high current harmonic content. Experimental results using a downscale prototype have been provided to confirm the correctness of the method. Construction of a full-scale prototype is ongoing.

REFERENCES

[1] M. Oettmeier, M. Spichartz, V. Staudt, and A. Steimel, "Test-bench set-up for high-power PMSM test drive for validating novel control schemes," in *Proc. 13th Int. Conf. Optim. Electr. Electron. Equip. (OPTIM)*, May 2012, pp. 509–514, doi: 10.1109/OPTIM.2012.6231803.

[2] S. Uebener and J. Böcker, "Application of an e-machine emulator for power converter tests in the development of electric drives," in *Proc. Eur. Electr. Vehicle Congr. (EEVC)*, Brussels, Belgium, 2012, pp. 582–588.

[3] J. Shen, S. Schröder, B. Qu, Y. Zhang, F. Zhang, K. Chen, and R. Zhang, "A high-frequency high-power test bench for 11 MW/595 Hz drives with 1.25 MW grid capability," *IEEE Trans. Ind. Appl.*, vol. 53, no. 5, pp. 4744–4756, Oct. 2017, doi: 10.1109/TIA.2017.2713758.

[4] J. Noon, H. Song, B. Wen, I. Cvetkovic, S. Srdic, G. Pammer, and R. Burgos, "Design and evaluation of a power hardware-in-the-loop machine emulator," in *Proc. IEEE Energy Convers. Congr. Expo. (ECCE)*, Oct. 2020, pp. 2013–2019, doi: 10.1109/ECCE44975.2020.9235711.

[5] K. S. Amitkumar, R. S. Kaarthik, and P. Pillay, "A versatile power-hardware-in-the-loop-based emulator for rapid testing of transportation electric drives," *IEEE Trans. Transport. Electrific.*, vol. 4, no. 4, pp. 901–911, Dec. 2018, doi: 10.1109/TTE.2018.2857216.

[6] M. Fischer, D. Erthle, P. Ziegler, J. Ruthardt, and J. Roth-Stielow, "Comparison of two power electronic topologies for power hardware in the loop machine emulator," in *Proc. IEEE Appl. Power Electron. Conf. Expo. (APEC)*, Mar. 2020, pp. 2950–2954, doi: 10.1109/APEC39645.2020.9124094.

[7] K. Saito and H. Akagi, "A real-time real-power emulator of a medium-voltage high-speed induction motor loaded with a centrifugal compressor," *IEEE Trans. Ind. Appl.*, vol. 55, no. 5, pp. 4821–4833, Sep. 2019, doi: 10.1109/TIA.2019.2928498.

[8] Z. Nie, X. Xiao, R. McMahon, P. Clifton, Y. Wu, and S. Shao, "Emulation and control methods for direct drive linear wave energy converters," *IEEE Trans. Ind. Informat.*, vol. 9, no. 2, pp. 790–798, May 2013, doi: 10.1109/TII.2012.2224120.

[9] M. Oettmeier, R. Bartelt, C. Heising, V. Staudt, A. Steimel, S. Tietmeyer, B. Bock, and C. Doerlemann, "Machine emulator: Power-electronics based test equipment for testing high-power drive converters," in *Proc. 12th Int. Conf. Optim. Electr. Electron. Equip.*, May 2010, pp. 582–588, doi: 10.1109/OPTIM.2010.5510537.

[10] Q.-C. Zhong and G. Weiss, "Synchronverters: Inverters that mimic synchronous generators," *IEEE Trans. Ind. Electron.*, vol. 58, no. 4, pp. 1259–1267, Apr. 2011, doi: 10.1109/TIE.2010.2048839.

[11] J. H. Jeon, J.-Y. Kim, H.-M. Kim, S.-K. Kim, C. Cho, J.-M. Kim, J.-B. Ahn, and K.-Y. Nam, "Development of hardware in-the-loop simulation system for testing operation and control functions of microgrid," *IEEE Trans. Power. Electron.*, vol. 25, no. 12, pp. 2919–2929, Dec. 2010, doi: 10.1109/TPEL.2010.2078518.

[12] M. Kesler, E. Ozdemir, M. C. Kisacikoglu, and L. M. Tolbert, "Power converter-based three-phase nonlinear load emulator for a hardware testbed system," *IEEE Trans. Power Electron.*, vol. 29, no. 11, pp. 5806–5812, Nov. 2014, doi: 10.1109/TPEL.2014.2301815.

[13] K. Ma, J. Wang, X. Cai, and F. Blaabjerg, "AC grid emulations for advanced testing of grid-connected converters—An overview," *IEEE Trans. Power Electron.*, vol. 36, no. 2, pp. 1626–1645, Feb. 2021, doi: 10.1109/TPEL.2020.3011176.

[14] J. Wang, L. Yang, Y. Ma, J. Wang, L. M. Tolbert, F. Wang, and K. Tomsovic, "Static and dynamic power system load emulation in a converter-based reconfigurable power grid emulator," *IEEE Trans. Power. Electron.*, vol. 31, no. 4, pp. 3239–3251, Apr. 2016, doi: 10.1109/TPEL.2015.2448548.

[15] J. D. Boles, Y. Ma, J. Wang, D. Osipov, L. M. Tolbert, and F. Wang, "Converter-based emulation of battery energy storage systems (BESS) for grid applications," *IEEE Trans. Ind. Appl.*, vol. 55, no. 4, pp. 4020–4032, Jul. 2019, doi: 10.1109/TIA.2019.2914421.

[16] J. Wang, Y. Ma, L. Yang, L. M. Tolbert, and F. Wang, "Power converter-based three-phase induction motor load emulator," in *Proc. 28th Annu. IEEE Appl. Power Electron. Conf. Expo. (APEC)*, Mar. 2013, pp. 3270–3274, doi: 10.1109/APEC.2013.6520769.

[17] Y. Boukadida, F. Marignetti, G. M. Casolino, A. Masmoudi, A. Andreoli, and M. Albanesi, "Emulation and testing for automotive propulsion drive using two cascaded inverters," *IEEE Trans. Ind. Appl.*, vol. 56, no. 2, pp. 1766–1783, Mar. 2020, doi: 10.1109/TIA.2019.2959756.

[18] A. H. Kadam, R. Menon, and S. S. Williamson, "A novel bidirectional three-phase AC-DC/DC-AC converter for PMSM virtual machine system with common DC bus," in *Proc. IEEE Appl. Power Electron. Conf. Expo. (APEC)*, Mar. 2018, pp. 1944–1951, doi: 10.1109/APEC.2018.8341284.

[19] B. Zhang, H.-N. Chiu, and Y.-M. Chen, "Coupling network state equation control for permanent magnet synchronous motor emulators," in *Proc. IEEE Int. Future Energy Electron. Conf. (IFEEC)*, Nov. 2021, pp. 1–5, doi: 10.1109/IFEEC53238.2021.9662007.

[20] L. Buhrkall, "Traction system case study," in *Proc. 9th Inst. Eng. Technol. Prof. Develop. Course Electr. Traction Syst.*, 2006, pp. 53–71.

[21] M. Steczek, P. Chudzik, and A. Szelag, "Combination of SHE- and SHM-PWM techniques for VSI DC-link current harmonics control in railway applications," *IEEE Trans. Ind. Electron.*, vol. 64, no. 10, pp. 7666–7678, Oct. 2017, doi: 10.1109/TIE.2017.2694357.

[22] Z. Zhao, Y. Zhong, H. Gao, L. Yuan, and T. Lu, "Hybrid selective harmonic elimination PWM for common-mode voltage reduction in three-level neutral-point-clamped inverters for variable speed induction drives," *IEEE Trans. Ind. Electron.*, vol. 27, no. 3, pp. 1152–1158, Mar. 2012, doi: 10.1109/TPEL.2011.2162591.

[23] A. F. Abouzeid, J. M. Guerrero, A. Endemaño, I. Muniategui, D. Ortega, I. Larrazabal, and F. Briz, "Control strategies for induction motors in railway traction applications," *Energies*, vol. 13, no. 3, p. 700, Feb. 2020, doi: 10.3390/en13030700.

[24] K. Ma and Y. Song, "Power-electronic-based electric machine emulator using direct impedance regulation," *IEEE Trans. Power Electron.*, vol. 35, no. 10, pp. 10673–10680, Oct. 2020, doi: 10.1109/TPEL.2020.2976143.

[25] A. F. Abouzeid, J. M. Guerrero, I. Vicente-Makazaga, I. Muniategui-Aspiazu, A. Endemano-Isasi, and F. Briz, "Torsional vibration suppression in railway traction drives," *IEEE Access*, vol. 10, pp. 32855–32869, 2022, doi: 10.1109/ACCESS.2022.3162415.

[26] X. Zou, X. Xiao, P. He, and Y. Song, "Permanent magnet synchronous machine emulation based on power hardware-in-the-loop simulation," in *Proc. IEEE Int. Electr. Mach. Drives Conf. (IEMDC)*, May 2019, pp. 248–253, doi: 10.1109/IEMDC.2019.8785386.

[27] R. Wu, J. L. Wen, J. Han, Z. Chen, Q. Wei, N. Jia, and C. Wang, "A power loss calculation method of IGBT three-phase SPWM converter," in *Proc. 2nd Int. Conf. Intell. Syst. Design Eng. Appl.*, Jan. 2012, pp. 1180–1183, doi: 10.1109/ISdea.2012.554.

[28] D. Zhou, Y. Peng, F. Iannuzzo, M. Hartmann, and F. Blaabjerg, "Thermal mapping of power semiconductors in H-bridge circuit," *Appl. Sci.*, vol. 10, no. 12, p. 4340, 2020. [Online]. Available: https://www.mdpi.com/2076-3417/10/12/4340, doi: 10.3390/app10124340.

[29] H. Yang, Y. Zhang, G. Yuan, P. D. Walker, and N. Zhang, "Hybrid synchronized PWM schemes for closed-loop current control of high-power motor drives," *IEEE Trans. Ind. Electron.*, vol. 64, no. 9, pp. 6920–6929, Sep. 2017, doi: 10.1109/TIE.2017.2686298.

[30] T. Tang, B. Yu, H. Cui, N. Wang, and W. Song, "Selective harmonic elimination PWM switching principle in multi-mode modulation for five-phase permanent magnet synchronous motors," in *Proc. 14th IEEE Conf. Ind. Electron. Appl. (ICIEA)*, Jun. 2019, pp. 1156–1161, doi: 10.1109/ICIEA.2019.8834001.

[31] *Electric Traction—Rotating Electrical Machines for Rail and Road Vehicles—Part 4: Permanent Magnet Synchronous Electrical Machines Connected to an Electronic Converter*, Standard IEC 60349-4:2012, International Electrotechnical Commission, 2012.
[32] S. Bhalerao, S. Pawar, and N. Patwardhan, "Design and implementation of bipolar SHE-PWM single phase inverter for lower order harmonic suppression," in *Proc. 3rd IEEE Int. Conf. Recent Trends Electron., Inf. Commun. Technol. (RTEICT)*, May 2018, pp. 1066–1071, doi: 10.1109/RTEICT42901.2018.9012349.
[33] Y. Sahali and M. Fellah, "Selective harmonic eliminated pulse-width modulation technique (SHE PWM) applied to three-level inverter/converter," in *Proc. IEEE Int. Symp. Ind. Electron.*, vol. 2, Jun. 2003, pp. 1112–1117, doi: 10.1109/ISIE.2003.1267980.

FERNANDO BRIZ (Senior Member, IEEE) received the M.S. and Ph.D. degrees from the University of Oviedo, Gijón, Spain, in 1990 and 1996, respectively. He is currently a Full Professor with the Department of Electrical, Computer and Systems Engineering, University of Oviedo. His research interests include electronic power converters and AC drives, power systems, machine monitoring and diagnostics, and digital signal processing. He is a member of the Executive Board of ECCE. He was a recipient of the IEEE TRANSACTIONS ON INDUSTRY APPLICATIONS Award and the nine IEEE Industry Applications Society Conference and IEEE Energy Conversion Congress and Exposition Prize Paper Award. He is the Chair of the Industrial Power Conversion System Department (IPCSD) of the IAS. He is the Past Chair of the Industrial Drives Committee of IPCSD. He has served for Scientific Committees and the Vice Chair or the Technical Program Chair for several conferences, including ECCE, IEMDC, ICEM, ICEMS, and SLED. He is the Deputy Editor-in-Chief and a member of the Steering Committee of IEEE JOURNAL OF EMERGING AND SELECTED TOPICS IN POWER ELECTRONICS. He is an Associate Editor of IEEE TRANSACTIONS ON INDUSTRY APPLICATIONS.

MARIAM SAEED (Member, IEEE) received the B.Sc. degree in electrical engineering from the University of Ain Shams, Cairo, Egypt, in 2013, and the M.Sc. and Ph.D. degrees in electrical engineering from the University of Oviedo, Gijón, Spain, in 2015 and 2020, respectively. She is currently a Postdoctoral Researcher with the Department of Electrical, Computer and Systems Engineering, University of Oviedo. Her research interests include electronic power converters, energy storage systems, and high frequency transformers.

JUAN MANUEL GUERRERO (Senior Member, IEEE) received the M.E. degree in industrial engineering and the Ph.D. degree in electrical and electronic engineering from the University of Oviedo, Gijón, Spain, in 1998 and 2003, respectively. Since 1999, he has been occupied different teaching and research positions with the Department of Electrical, Computer and Systems Engineering, University of Oviedo, where he is currently a Full Professor. From February 2002 to October 2002, he was a Visiting Scholar at the University of Wisconsin, Madison. From June 2007 to December 2007, he was a Visiting Professor at Tennessee Technological University, Cookeville. His research interests include control of electric drives and power converters, electric traction, and renewable energy generation. He is an Associate Editor of the IEEE TRANSACTIONS ON INDUSTRY APPLICATIONS.

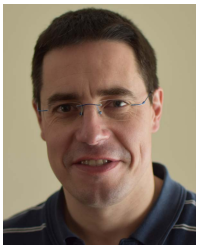

IGOR LARRAZABAL received the M.Sc. degree in electrical engineering from the Institut Nationale Polytechnique of Toulouse (INPT), France, in 1998. He worked with the Traction Department of Ingeteam, from 1998 to 2008, when he joined the Windpower Department of Ingeteam. In 2016, he joined the Traction Department again, where he is currently the Product Development Director. His research interests include the field of railway applications, traction chains, and power converters.

DAVID ORTEGA received the Licentiate degree in electrical and electronic engineering from the Universidad Pais Vasco of Bilbao (UPV), Spain, in 2004. He worked with the Traction Department of Ingeteam, from April 2004 to April 2010, as a Development Engineer, when he joined Euskotren as a Rolling Stock Maintenance Engineer. Later in December 2010, he joined again the Traction Department of Ingeteam, where he is currently the Technology Coordination Manager. His research interests include the field of rolling stock architectures, EMC, noise, efficiency, and high power converters for traction and energy recovery systems.

IBAN AYARZAGUENA received the Licentiate degree in industrial automation from the Mondragon Unibertsitatea of Mondragon (MU), Spain, in 2007. He has been working with the Traction Department of Ingeteam, since 2007, where he is currently a Power Electronics Engineer. His research interests include the field of semiconductors, drivers, capacitors, and power stacks.

ANDONI PULIDO received the degree in electrical engineering and the degree in industrial electronics from the University School of Industrial Technical Engineering (EUITI), Bilbao, Spain, in 2013 and 2018, respectively, and the master's degree in energy and power electronics from Mondragon University (MU), Spain. He continued with his studies in industrial electronics and, in 2015, started working at Elytt Energy, designing and manufacturing a resin impregnation machine for ITER Poloidal Field Coils. The final degree project was based on a study and design of an induction coil with a resonant converter for metal hardening. He joined the Traction Department of Ingeteam, focusing on the design of test benches for power electronics modules.